NANO · MICRO small
www.small-journal.com

Charge Storage Mechanism in Electrospun Spinel-Structured High-Entropy $(Mn_{0.2}Fe_{0.2}Co_{0.2}Ni_{0.2}Zn_{0.2})_3O_4$ Oxide Nanofibers as Anode Material for Li-Ion Batteries

Claudia Triolo, Mariam Maisuradze, Min Li, Yanchen Liu, Alessandro Ponti, Gioele Pagot, Vito Di Noto, Giuliana Aquilanti, Nicola Pinna, Marco Giorgetti,* and Saveria Santangelo**

High-entropy oxides (HEOs) have emerged as promising anode materials for next-generation lithium-ion batteries (LIBs). Among them, spinel HEOs with vacant lattice sites allowing for lithium insertion and diffusion seem particularly attractive. In this work, electrospun oxygen-deficient (Mn,Fe,Co,Ni,Zn) HEO nanofibers are produced under environmentally friendly calcination conditions and evaluated as anode active material in LIBs. A thorough investigation of the material properties and Li^+ storage mechanism is carried out by several analytical techniques, including ex situ synchrotron X-ray absorption spectroscopy. The lithiation process is elucidated in terms of lithium insertion, cation migration, and metal-forming conversion reaction. The process is not fully reversible and the reduction of cations to the metallic form is not complete. In particular, iron, cobalt, and nickel, initially present mainly as Fe^{3+}, Co^{3+}/Co^{2+}, and Ni^{2+}, undergo reduction to Fe^0, Co^0, and Ni^0 to different extent (Fe < Co < Ni). Manganese undergoes partial reduction to Mn^{3+}/Mn^{2+} and, upon re-oxidation, does not revert to the pristine oxidation state (+4). Zn^{2+} cations do not electrochemically participate in the conversion reaction, but migrating from tetrahedral to octahedral positions, they facilitate Li-ion transport within lattice channels opened by their migration. Partially reversible crystal phase transitions are observed.

1. Introduction

In recent decades, the widespread use of lithium ion batteries (LIBs) in portable electronic devices and electric vehicles has promoted a relentless search for anode materials alternative to graphite, the latter having high reversibility and low cost, but limited capacity (372 mAh g^{-1}). Transition metal (TM) oxide-based conversion anodes, with a much higher theoretical capacity (600–1200 mAh g^{-1}[1–3]), have been extensively studied and have emerged as promising alternatives for next generation LIBs. Unfortunately, they suffer from poor conductivity and large volume expansion during cycling, which causes severe decay in capacity. Recently, using the concept of high entropy, a new class of materials has been developed, based on single-phase multi-element solid solutions.[4,5] High-entropy materials, comprising alloys,[4,5] oxides,[6–9] nitrides,[10] carbides,[11] sulfides,[12] and other compounds[13] with a variety of

C. Triolo, S. Santangelo
Dipartimento di Ingegneria Civile, dell'Energia, dell'Ambiente e dei Materiali (DICEAM)
Università "Mediterranea,"
Via Zehender, Loc. Feo di Vito, Reggio Calabria 89122, Italy
E-mail: saveria.santangelo@unirc.it

The ORCID identification number(s) for the author(s) of this article can be found under https://doi.org/10.1002/smll.202304585

DOI: 10.1002/smll.202304585

C. Triolo, M. Maisuradze, M. Li, G. Pagot, V. Di Noto, M. Giorgetti, S. Santangelo
National Reference Center for Electrochemical Energy Storage (GISEL)
Consorzio Interuniversitario Nazionale per la Scienza e Tecnologia dei Materiali (INSTM)
Firenze 50121, Italy
E-mail: marco.giorgetti@unibo.it

M. Maisuradze, M. Li, M. Giorgetti
Department of Industrial Chemistry "Toso Montanari"
University of Bologna
Viale del Risorgimento 4, Bologna 40136, Italy

Y. Liu, N. Pinna
Department of Chemistry
IRIS Adlershof & The Center for the Science of Materials Berlin
Humboldt-Universität zu Berlin
Brook-Taylor-Str. 2, 12489 Berlin, Germany
E-mail: nicola.pinna@hu-berlin.de

lattice structures (perovskite, spinel, rock-salt, etc.), show enhanced properties and potential for application in a large variety of different fields,[13,14] including rechargeable alkali metal-ion batteries.[7,15–20] Specially, rock salt-structured $(Mg_{0.2}Co_{0.2}Ni_{0.2}Cu_{0.2}Zn_{0.2})O$, the first single-phase synthesized in 2015 via solid-state reaction,[6] has been the focus of extensive research work[7,15,16,21–25] and its superior properties in lithium-storage have been reported by many groups.[7,15,16,21,22,24–26] Based on the results of ex situ and in operando X-ray absorption spectroscopy (XAS) at the Co, Ni, and Cu K-edges, it has been proposed that the lithiation of $(Mg_{0.2}Co_{0.2}Ni_{0.2}Cu_{0.2}Zn_{0.2})O$ involves reduction of Co^{2+}, Ni^{2+}, Cu^{2+}, and Zn^{2+} cations in the reaction $MO + 2Li^+ + 2e^- \rightarrow M + Li_2O$,[21] while spectator Mg^{2+} preserves the rock-salt structure during lithiation.[15,21,22]

By replacing Co and Ni with Ti and Fe or Mg and Zn with Mn and Fe, spinel-structured $(Mg_{0.2}Ti_{0.2}Fe_{0.2}Cu_{0.2}Zn_{0.2})_3O_4$[27] and $(Mn_{0.2}Fe_{0.2}Ni_{0.2}Cu_{0.2}Zn_{0.2})_3O_4$[28] single-phases are obtained. Spinel-structured HEOs are more promising candidates as anode materials since they have higher Li^+-storage capacity compared to rock-salt oxides.[29] Among them, $(Cr_{0.2}Mn_{0.2}Fe_{0.2}Co_{0.2}Ni_{0.2})_3O_4$, first synthesized in 2018 via a solid-state method,[30] has received great attention.[31–38] A charge/discharge capacity of 1235 mAh g^{-1} (at 20 mA g^{-1}), the highest among all known HEOs, has been reported for $(Cr_{0.2}Mn_{0.2}Fe_{0.2}Co_{0.2}Ni_{0.2})_3O_4$ nanoparticles synthesized via a surfactant-assisted hydrothermal method[35] (Cr,Mn,Fe,Co,Ni) HEO prepared by the oxidation of high-entropy CrMnFeCoNi alloy powders delivers a reversible capacity of 597 mAh g^{-1} and shows a capacity retention of 86% after 1200 cycles at 2 A g^{-1}.[39] The stability of $(Cr_{0.2}Mn_{0.2}Fe_{0.2}Co_{0.2}Ni_{0.2})_3O_4$ synthesized by solid state reaction (402 mAh g^{-1} capacity after 300 cycles at 0.5 A g^{-1}) has been attributed to the amorphization process occurred during the initial discharging.[31] Oxygen-deficient spinel-type (Cr,Mn,Fe,Co,Zn) HEO prepared via ball milling exhibits a discharge capacity of 828.6 mAh g^{-1} at 2.0 A g^{-1} after 2000 cycles.[40] Spinel-structured (Ti,Mn,Fe,Co,Ni) HEO produced by solid-state sintering shows a reversible capacity of 560 mAh g^{-1} with a higher capacity retention than other micro-sized conversion-type TM oxides (100% after 100 cycles at 0.1 A g^{-1}).[41] Its charge storage mechanism has been investigated by a combination of techniques including operando synchrotron XAS. The results have indicated that Ni, Co, Mn, and Fe ions are reduced to the metal state during the lithiation process, while Ti ions form $LiTi_2O_4$, according to the reaction $(Ni_{0.2}Co_{0.2}Mn_{0.2}Fe_{0.2}Ti_{0.2})_3O_4 + 5.9Li^+ + 5.9e^- + \rightarrow 0.6Ni + 0.6Co + 0.6Mn + 0.6Fe + 0.3LiTi_2O_4 + 2.8Li_2O$, which helps to stabilize the spinel structure.[41]

Very recently, it has been shown that electrospinning, a versatile, cost-effective and scalable technique, suitable for the large-scale production,[42–44] allows obtaining single-phase HEOs in the form of nanofibers (NFs)[24,25,45–47] under milder conditions (shorter heat treatments at lower temperatures) than standard solid-state techniques.[25,47,48] Anodes based on both rock-salt $(Mg_{0.2}Co_{0.2}Ni_{0.2}Cu_{0.2}Zn_{0.2})O$[25] and spinel $(Cr_{0.2}Mn_{0.2}Fe_{0.2}Co_{0.2}Zn_{0.2})_3O_4$[47] HEO NFs show greater stability and higher reversible capacity than those prepared with HEO nanoparticles (NPs) synthesized by conventional sol–gel method.[25,47] Nevertheless, a previous study[36] has highlighted the presence of Cr^{6+} species, having toxic effects when inhaled or ingested, on the surface of spinel-structured $(Cr_{0.2}Mn_{0.2}Fe_{0.2}M'_{0.2}M''_{0.2})_3O_4$ NFs (where M′ is Co or Ni, and M″ is Ni or Zn, respectively), in agreement with other studies.[35]

In this work, electrospun HEO NFs based on a Cr-free combination of five metals, namely (Mn, Fe, Co, Ni, Zn) are produced and evaluated as anode active material in LIBs. To prevent the formation of secondary phases[49] previously observed by calcining for 4 h of which 2 h at 900 °C,[47] calcination is here carried out at lower temperature (700 °C) for a shorter time (only 30 min), with benefits both in terms of environmental impact of the production process and sintering effects on the size of the oxide grains forming the NFs, and possibly also in terms of electrode performance.[24] An in-depth investigation of the material properties and mechanism of Li^+ storage is carried out using a combination of analytical techniques including ex situ synchrotron XAS.[50] By XAS it is possible to probe the local chemical environment of atoms and their oxidation states. As a bulk technique, XAS provides representative information about the whole sample.

2. Results and Discussion

2.1. Morphology, Texture, Microstructure, Crystalline Phase and Surface Composition of the Pristine NFs

Figure 1 shows the main results of scanning electron microscopy (SEM), high-resolution transmission electron microscopy (HRTEM), energy dispersive X-ray spectroscopy (EDX), X-ray diffraction (XRD), micro-Raman spectroscopy (MRS), and X-ray photoelectron spectroscopy (XPS) analyses carried out to investigate the morphology, texture, microstructure, crystalline phase and surface composition of the (Mn,Fe,Co,Ni,Zn)-HEO NFs. SEM analysis (Figure 1a; Figure S1a,b, Supporting Information) reveals that straight NFs, 5–15 µm in length, form from the as-spun templates upon calcination. The NF diameter, nearly uniform along the fiber axis, has distributed peaked at 0.28 µm (Figure S1c, Supporting Information). TEM analysis confirms the morphology of the NFs (Figure S1d,e, Supporting Information), which have a granular architecture, as peculiar to both low-entropy[51–53] and high-entropy[25,36] electrospun oxide fibers. They consist of densely packed oxide grains (Figure 1b; Figure S1e, Supporting Information), having well-defined polyhedral shape with rounded vertices and size of a few tens of nm (Figure 1c). The opposite solicitations experienced by PAN and embedded acetates (expansion outward and contraction inward, respectively[23,54]) owing to the degradation of organic components of the pristine fibers during calcination is responsible for

A. Ponti
Laboratorio di Nanotecnologie
Istituto di Scienze e Tecnologie Chimiche "Giulio Natta" (SCITEC)
Consiglio Nazionale delle Ricerche
Via Fantoli 16/15, Milano 20138, Italy
G. Pagot, V. Di Noto
Department of Industrial Engineering
Section of Chemistry for the Technology (ChemTech)
University of Padova
Via Marzolo 9, Padova (PD) 35131, Italy
G. Aquilanti
Elettra Sincrotrone Trieste S.C.p.A.
s.s. 14 km 163.5, Basovizza, Trieste 34149, Italy

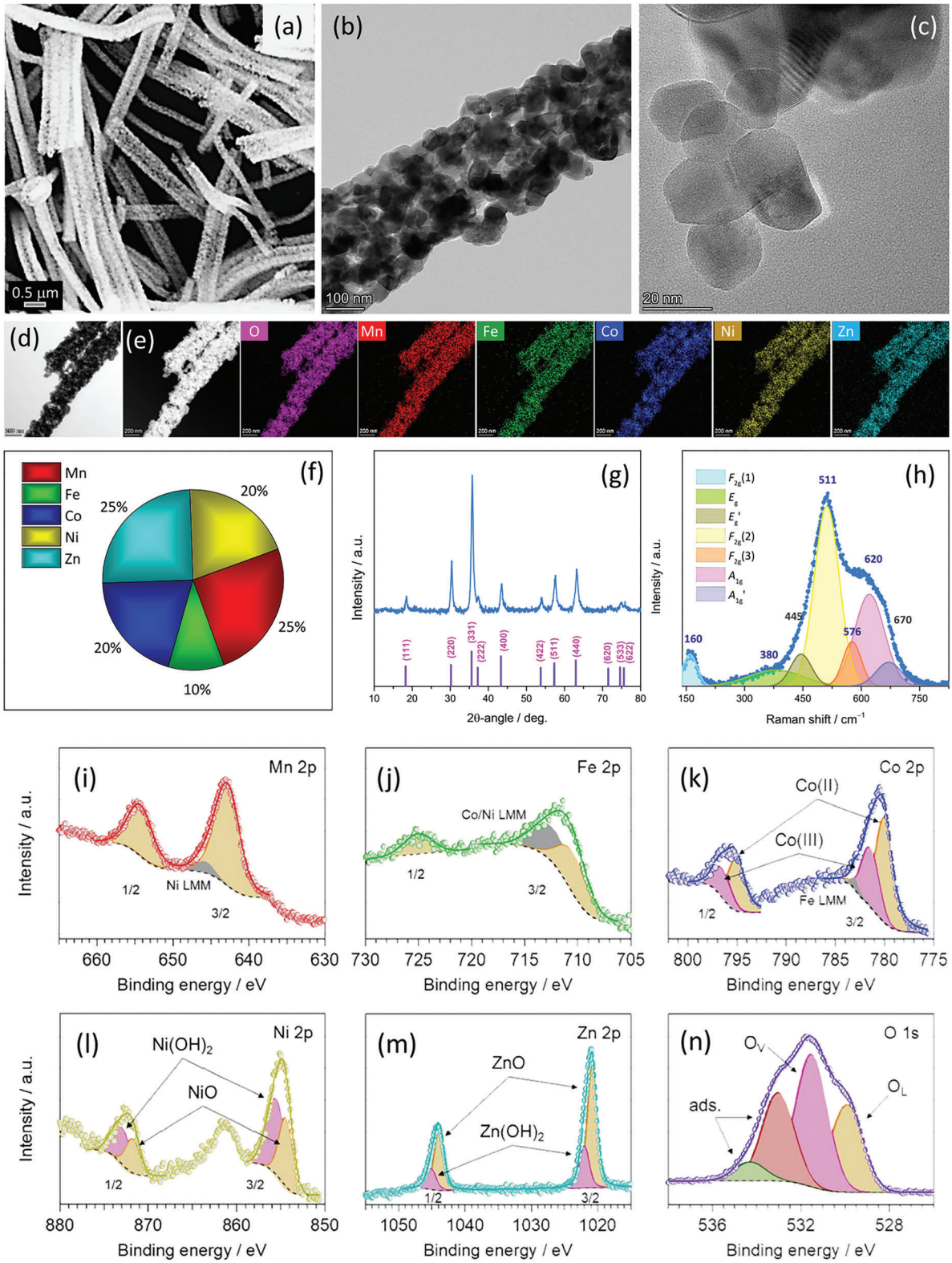

Figure 1. Results of the a) SEM, b–f) (S)TEM, g) XRD, h) micro-Raman, and i–n) XPS analyses. a) SEM, b) TEM, c) HRTEM, d) BF-STEM, and e) HAADF-STEM images; the latter is followed by STEM/EDX elemental maps and f) STEM/EDX relative concentration of the TMs; g) XRD pattern and h) micro-Raman spectrum fitted to Gaussian bands; i–n) results of the high-resolution XPS studies in the different spectral regions: i) Mn 2p, j) Fe 2p, k) Co 2p, l) Ni 2p, m) Zn 2p, and n) O 1s core levels.

the formation of space-confined oxide grains, whereas the interconnected metal-network built up via sol-chemistry from the reaction among five acetates gives rise to the multicomponent oxide. The HEO grains are crystalline in nature, as proved by the diffraction rings in the selected-area electron diffraction (SAED) patterns (Figure S1f, Supporting Information). They have spinel structure and are randomly oriented.

Geometrical phase analysis (GPA) of the crystal lattice fringes in the HRTEM images provides information about the crystallinity of the primary HEO nanoparticles (NPs) and the crystallographic relationship with neighboring particles (see Supporting Information and ref. [36] for further details). The results, shown in Figure S1i–n, Supporting Information, indicate that the primary NPs are single crystals and that some lattice strain affects those well inside the NFs.

Elemental mapping via STEM/EDX analysis (Figure 1d,e) proves the spatially uniform distribution of Mn, Fe, Co, Ni, Zn, and O throughout all NFs. Compositional analysis via STEM/EDX further evidences a deviation from the nominal (equimolar) TM combination (Figure 1f), leading to the composition $(Mn_{0.24}Fe_{0.11}Co_{0.21}Ni_{0.21}Zn_{0.23})_3O_4$.

Additional information on the NF morphology is obtained via projection analysis of STEM-EDX elemental maps (Figure S1g, Supporting Information), as described in detail in a previous paper.[36] The normalized profiles of Mn, Fe, Co, Ni, Zn, and O are superimposed within the experimental noise, confirming the homogeneity of the cation distribution within the oxide lattice; the fit of oxygen longitudinal projection to model profiles (see Supporting Information and ref. [36] for further details) indicates that the NFs are quasi solid (Figure S1h, Supporting Information). They have a narrow inner channel, whose size is about 20% of the outer diameter of the fibers. The formation of tube-like electrospun NFs has been previously reported for both low-entropy[51,53] and high-entropy[36] oxides. The hollow NF structure is due to the large temperature gradient along the radial direction experienced by the precursor PAN/metal-acetate(s) NFs owing to the rapid rise in temperature (10 °C min^{-1}) during calcination.[55] Under fixed calcination conditions, the relative size of the inner channel of the tube-like HEO NFs is composition-dependent.[36] Conversely, for a fixed HEO composition, it might change with calcination temperature as variation in calcination temperature promotes structural and morphological evolution of the fibers.[51]

In full agreement with information inferred from the SAED pattern, in the diffractogram of the (Mn,Fe,Co,Ni,Zn)-HEO NFs (Figure 1g), only the reflections from planes of the face-centered cubic (fcc) spinel structure (JCPDS no. 22-1084) are detected.[27,30–32,35,56,57] Rietveld refinements from XRD data (Figure S2a, Supporting Information) confirm the absence of secondary phase(s) and the formation of pure single-phase spinel. The average size of HEO crystallites is 59 nm. This value, comparable with the size of the NF grains, agrees well with the indication, emerged from GPA, that NFs are formed by interconnected single crystals.

MRS probes a smaller region (<0.6 μm^2) than XRD. Thus, measuring Raman scattering from different locations in the specimen allows evaluating its spatial homogeneity (Figure S2b, Supporting Information).[25,30] The lack of significant differences in the spectral profiles confirms the formation of a pure single-phase HEO.[25,30] Small differences in the peak widths might reflect a non-homogeneous distribution of lattice strains/defects (which inhomogeneously broadens the peaks[58]), in agreement with the outcomes of GPA. Figure 1h displays the micro-Raman spectrum obtained by averaging all collected spectra. Five Raman-active normal vibration modes ($A_{1g} + E_g + 3F_{2g}$) are predicted for the spinel structure (*Fd-3m* space group).[59–63] Their frequency positions and relative intensities depend on the radius of cations in the oxide lattice[61] and strongly vary within the family of spinels.[60,61,64–67] As shown in Figure 1h, seven Gaussian bands are required to reproduce the spectrum of HEO NFs. The bands centered at 160, 380, 511, 576, and 620 cm^{-1} are assigned to the normal $F_{2g}(1)$, E_g, $F_{2g}(2)$, $F_{2g}(3)$, and A_{1g} phonon modes, respectively.[36,47] The additional contributions to the Raman intensity located at 445 and 670 cm^{-1} are ascribed to the inversion-induced E_g' and A_{1g}' modes, respectively.[30,33,61,68] The detection of Raman-bands originating from inversion has been previously reported for both HEO NFs[36,47] and NPs[33,47] based on different combinations of metals.

XPS studies reveal that the surface of the sample is composed of Mn, Fe, Co, Ni, Zn, and O atoms (Table S1, Supporting Information). The relative abundance of the five TMs is 22.1, 6.5, 26.8, 19.5, and 25.1 at% for Mn, Fe, Co, Ni and Zn, respectively, indicating a deficiency of iron on the surface of this compound, in agreement with the results of the "bulk" elemental composition obtained by STEM/EDX. The other TMs have a similar concentration. XPS analyses allow for the determination of the oxidation states of the different elements composing the surface of the sample. Unfortunately, the presence of a large number of TMs limits the accuracy of data analysis, due to the overlapping of several Auger lines to the main spectral transitions of the investigated elements. The Mn 2p spectral region (Figure 1i) reveals the presence of three different peaks, attributed to: i) Mn $2p_{3/2}$ at ≈642.9 eV; ii) Mn $2p_{1/2}$ at ≈654.3 eV; and iii) Ni LMM Auger peaks at ≈645.8 eV.[69] The BE values of these peaks are in agreement with the presence of Mn(IV) species.[70] Two iron features are detected in the Fe 2p spectral region (Figure 1j), with the $2p_{3/2}$ and $2p_{1/2}$ peaks at ≈710.5 and 725.1 eV. In particular, these values are an indication of the presence of iron atoms in Fe(III) oxidation state, as in Fe_2O_3.[71] In addition, the Co and Ni LMM Auger lines appear in this spectrum.[69] Five peaks are detected in the Co 2p spectral region (Figure 3k), which are assigned to: i) the $2p_{3/2}$ features of Co^{2+} and Co^{3+}, peaking at ≈780.1 and 781.5, respectively;[72,73] ii) the $2p_{1/2}$ features of Co^{2+} and Co^{3+}, peaking at ≈795.2 eV and 796.6 eV, respectively;[72,73] and iii) the Fe LMM Auger line at ≈783.1 eV.[69] Nickel (Figure 1l) and zinc (Figure 1m) exhibit the presence of both metal oxide species and some hydroxide surface defects. In details, the $2p_{3/2}$ peaks of NiO and $Ni(OH)_2$ are observed at 854.5 and 855.6 eV, respectively,[74,75] while they are present at ≈1020.9 and 1022.1 eV in the case of zinc compounds.[76,77]

The analysis of the O 1s photo-peak is very useful to investigate and quantify the presence of oxygen vacancies on the surface of the analyzed sample.[36,48] In this region, four different peaks are detected (Figure 1n): i) at ≈530.0 eV the lattice O^{2-} ions (O_L) belonging to mixed TM oxides;[76,78–80] ii) at ≈531.5 eV the native defects of O^{2-} vacancies (O_V);[80–82] and iii) at higher BEs the adsorbed or chemisorbed oxygen species, such as O_2 or H_2O.[36,48,82] The peak

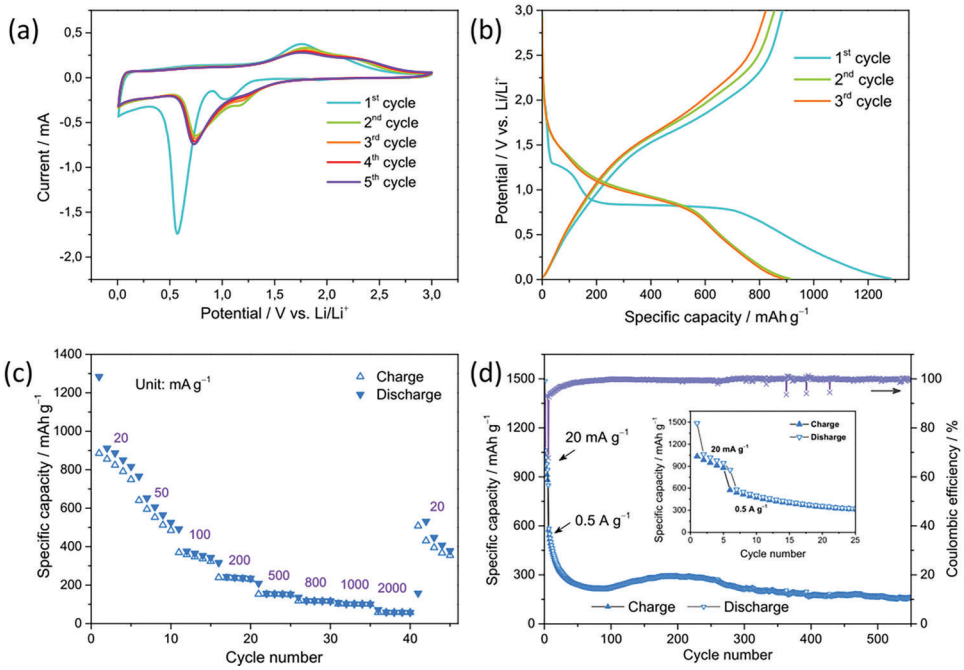

Figure 2. Electrochemical performance of the HEO NFs. a) CV curves (scanning rate of 0.1 mV s^{-1}), b) galvanostatic charge–discharge curves measured at 20 mA g^{-1}, c) rate capability, and d) cycling stability.

attributed to O_V species accounts for the 40.6% of the total oxygen signal (Table S2, Supporting Information). This value, higher than that previously observed in electrospun HEO NFs calcined at higher temperature,[36,48] is comparable to that reported for HEO prepared with different techniques.[40] The very high O_V concentration could be beneficial for lithium-ion diffusion during charge and discharge.[40]

2.2. Electrochemical Behavior in LIBs

The Li storage performance of (Mn,Fe,Co,Ni,Zn)-HEO NFs was investigated in half cells with Li anodes by recording galvanostatic charge-discharge (GCD) curves. Cyclic voltammetry (CV) was carried out to study the redox reactions and structural transformation during lithiation and de-lithiation process. **Figure 2**a displays the CV curves recorded in the 0.01–3.0 V potential range at a scan rate of 0.1 mV s^{-1}. In the first cathodic scan (lithiation), two peaks are detected at 0.57 and 1.0 V. They can be assigned to the formation of solid electrolyte interface (SEI) layer on the materials surface due to the decomposition of the electrolyte[15,21] and to the reduction reaction of electrochemically active cations along with the formation of Li_2O[7,21,27,83] and irreversible change of crystal structure.[27] In the subsequent anodic scan (de-lithiation), the peaks at 1.74 and 2.14 V can be ascribed to the re-oxidation process of the redox-active species along with the decomposition of Li_2O. In the following cycles, both the cathodic peaks at around 0.7/1.2 V and the anodic peaks at around 1.8/2.3 V appear well overlapping, evidencing the good reversibility of lithiation/de-lithiation in HEO NFs.

Figure 2b shows typical GCD curves of the first three cycles at 20 mA g^{-1}. The initial discharge and charge capacities of the HEO NFs are 1283.6 and 885.2 mA g^{-1}, respectively, corresponding to an initial Columbic efficiency (CE) of 69.0%. The capacity loss of the first cycle can be attributed to the decomposition of the electrolyte to form the SEI layer and the occurrence of irreversible structural rearrangements,[21,27] which is consistent with the long plateau at around 0.8 V during the lithiation process.

The rate capability of HEO NFs was evaluated by varying current density from 20 to 2000 mA g^{-1} (Figure 2c). At 20, 50, 100, 200, 500, 800, 1000, and 2000 mA g^{-1}, the lithiation capacities are 912, 653, 377, 237, 153, 118, 102, and 58 mAh g^{-1}, respectively. When the current density is set back to 20 mA g^{-1}, a capacity of 532 mAh g^{-1} is recovered. The granular architecture of the fibers and their inner channel, which facilitate the electrolyte filtration and, thus, shorten the diffusion path of Li ions and electrons are responsible for good rate capability.

Long-term cycling stability is a key factor for the practical use of LIBs. After 550 cycles at 0.5 A g^{-1} (Figure 2d), the electrode based on electrospun (Mn,Fe,Co,Ni,Zn) HEO NFs still delivers 155 mAh g^{-1}. This value exceeds that reported in the literature for commercial graphite (Table S3, Supporting Information) and is comparable with that previously obtained with anodes based on other spinel structured HEOs. The rapid decrease in capacity during the initial 80 cycles may originate from the irreversible structure transformation.[27] The non-monotonic trend of the specific capacity, featured by an increase after the initial decrease, followed by a new decrease before stabilizing at a constant value, is frequently observed in TM oxides[84] and is attributed to a possible activation process in the electrode,[85] due to the increase in interfaces.[86] Also CE increases to

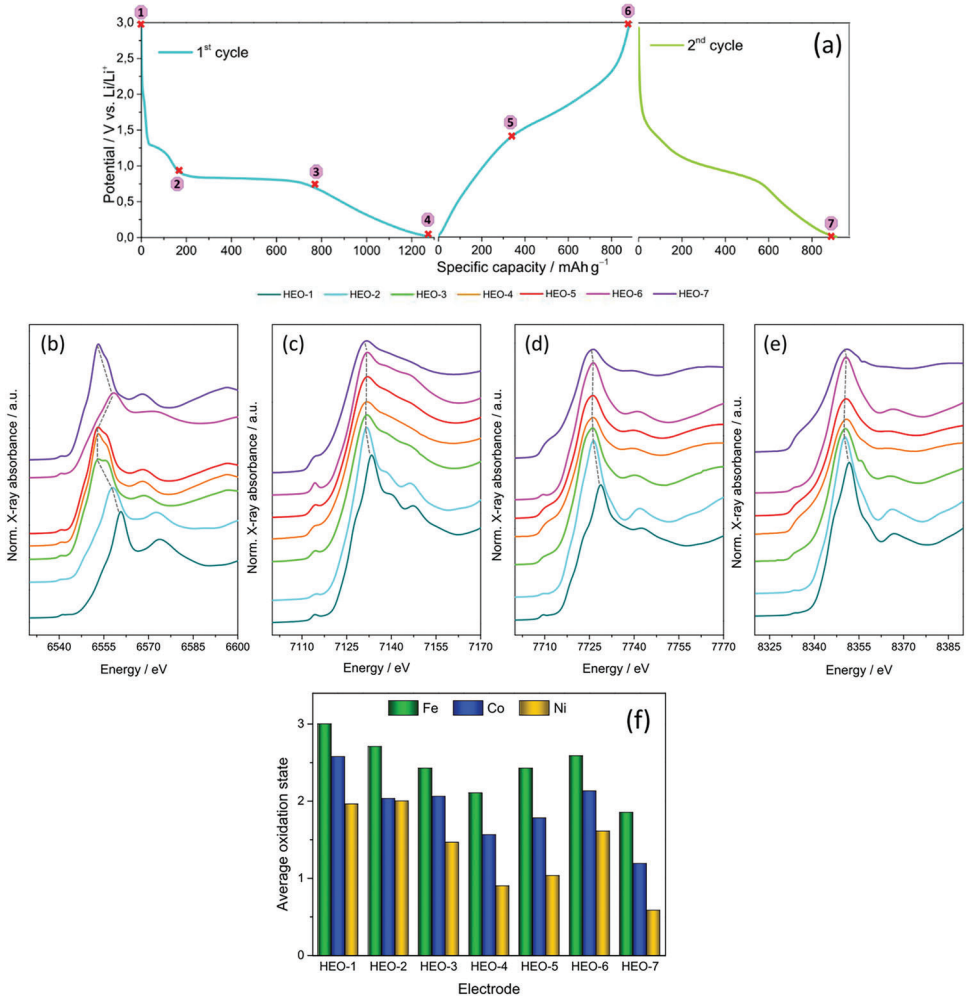

Figure 3. a) Different states of charge (SOC) of the electrodes extracted from LIBs: 1) OCP, 2) discharge to 0.9 V, 3) discharge to 0.7 V, 4) discharge to 0.01 V, 5) charge to 1.4 V, 6) charge to 3V, and 7) 2nd discharge to 0.01 V. Normalized XANES spectra recorded at b) Mn, c) Fe, d) Co, and e) Ni K-edges in electrodes with different SOC. Spectra are translated vertically for easier comparison and dashed lines are drawn to highlight the peak shifts. f) Average oxidation state of Fe, Co, and Ni in electrodes with different SOC.

≈99% after about 50 cycles and remains stable over subsequent cycles.

2.3. Results of Ex Situ XAS Analysis and Charge Storage Mechanism

In order to understand the mechanism of lithium storage in the (Mn,Fe,Co,Ni,Zn)-HEO NFs and investigate the reversibility of the process, the ex-situ XAS analysis was carried out on the HEO-based electrodes extracted from LIBs in different states of charge (SOC, **Figure 3**a). Hereafter, the fresh electrode is coded as HEO-0, those extracted from LIBs in different states of charge are labelled as HEO-1 (open circuit potential, OCP, 3.0 V), HEO-2 (discharged to 0.9 V), HEO-3 (discharged to 0.7 V), HEO-4 (discharged to 0.01 V), HEO-5 (charged to 1.4 V), HEO-6 (charged to 3V), and HEO-7 (discharged to 0.01 V, in the 2nd cycle).

Due to the high selectivity for the atomic species, combined with the bulk sensitivity, the XAS probe can reveal key information, such as local structural changes and different degrees of charge of metals in electrodes with different SOC. Below, the structural and charge analysis of the pristine electrode is first presented, followed by analysis on electrodes with different SOC.

2.3.1. Pristine Electrode

Figure S3, Supporting Information, compares the normalized X-ray absorption near edge structure (XANES) spectra recorded at all metal K-edges in the fresh electrode (HEO-0) and in electrode HEO-1 (SOC: OCP). The lack of differences between the spectra of the two electrodes indicates that no change occurs in the HEO structure when the electrode is placed in contact with the electrolyte solution.

In order to get a deeper insight into the structure and different degrees of charge of metals, the XANES spectra of the fresh electrode are compared with metal foil and/or oxide standards for Mn, Fe, Co, Ni, and Zn K-edges (Figure S4, Supporting

Information). Since oxygen is the first shell coordination in all metal-core, this choice is the most suitable one. Each part of the spectra needs to be carefully examined. Although higher transition energies are generally associated with higher valence states of elements, neighboring atoms and local atomic geometry also strongly influence the spectra.

XANES spectra recorded at Mn, Fe, Co, and Ni K-edges (Figure S4a–d, Supporting Information) are characterized by a pre-edge peak on the lower energy side. The peak, slightly more defined in the case of cobalt and iron, is due to the 1s → 3d transition. Its presence indicates a distortion of the metal site, suggesting that all metals can be in both tetrahedral and octahedral positions, in agreement with literature reports on other spinel-structured HEOs.[41]

Going into more detail, to some extent, the Mn K-edge (E_0=6553.4 eV) in the fresh electrode resembles the Mn K-edge spectrum of MnO_2 (Figure S4a, Supporting Information). It can be argued that manganese is mainly in the +4-oxidation state. However, the shoulder at 6573.9 eV suggests a similarity with Mn K-edge spectrum of Mn_2O_3 oxide, hinting the possible coexistence of Mn^{3+} cations in the fresh electrode. The Fe K-edge (Figure S4b, Supporting Information) closely resembles the Fe K-edge spectrum of γ-Fe_2O_3. This similarity indicates that, at the beginning of the battery operation, iron is in the 3+-oxidation state. The Co K-edge exhibits a strong similarity with that of Co_3O_4 (Figure S4c, Supporting Information), even if with slightly shifted edge maxima. This suggests the presence of both Co^{2+} and Co^{3+} cations. Although the Ni K-edge closely resembles that of NiO (Figure S4d, Supporting Information), indicating the presence of Ni^{2+} cations, the initial value of E_0 and pre-edge structures suggest that it is likely that Ni^{3+} cations are also present (to a small extent), as in the case of cobalt. These findings are consistent with the increasing electronegativity in the order Mn < Fe < Co < Ni.[36]

Finally, the Zn K-edge in the fresh electrode (Figure S4e, Supporting Information) resembles the Zn K-edge spectrum of $ZnFe_2O_4$,[87] which belongs to the class of normal spinels. Hence, oxidation state of zinc is 2+ and Zn^{2+} cations are expected to occupy tetrahedral 8*a* sites. As 1s → 3d transition is forbidden for the $3d^{10}$ configuration of Zn^{2+} cations, no pre-edge peak can be detected. These findings substantially agree with the indications about the oxidation state of the TMs in the fresh electrode that emerged from the XPS analysis.

2.3.2. Electrode at Different SOC

Figure 3b–e displays the normalized XANES spectra recorded at Mn, Fe, Co, and Ni K-edges in electrodes with different SOC. Overall, all metals appear to be electroactive in the electrochemical process although they play a different role in the charge storage process. Some metals contribute more than others, as evidenced by the larger changes in edge energy, while others exhibit more severe structural changes upon oxidation and reduction (see also the Fourier transform behavior of the EXAFS portion, below). Generally speaking, since in electrodes from HEO-1 to HEO-4 the edge energy moves toward lower values, it can be argued that a progressive reduction in metal valence-state occurs, as expected. Then, oxidation is observed in spectra of electrodes HEO-5 and HEO-6 and again a reduction in HEO-7. A deeper insight into the structure and different degrees of charge of Mn, Fe, Co and Ni is obtained by comparing the spectra of electrodes at different SOC with those of metal foil and/or oxide standards for the corresponding K edges (Figure S5, Supporting Information).

With the reduction of the electrode, Mn^{2+} cations begin to appear in the structure; even if the edge energy is higher than that of pure manganese (II)-oxide, already in the electrode discharged to 0.9 V (HEO-2, Figure S5a, Supporting Information), the shape of the spectrum has an undeniable resemblance with that of Mn K-edge in MnO standard. The oxidation that occurs in HEO-6 causes the edge to shift back to higher energy, near the value of manganese in Mn_3O_4, whereas also some features peculiar to Mn_2O_3 oxide standard become visible (Figure S5i, Supporting Information). Mn^{4+} cations no longer appear in the oxidized sample, indicating that the process is only partially reversible and the initial structure is not fully recovered. This finding is in agreement with the difference between first and subsequent discharge curves (Figure 2a).

The shift in the edge energy position of the Fe K-edge, observed in electrode HEO-2 (Figure S5b, Supporting Information), suggests the additional contribution by Fe^{2+} along with Fe^{3+} cations. At the first glance, electrodes HEO-4 and HEO-6 have quite similar patterns, but the increase in intensity of the pre-edge peak, together with the weakening of the most intense peak, suggests a contribution by metallic iron (Figure S5f,j, Supporting Information).

In the Co K-edge spectrum of HEO-2 (Figure S5c, Supporting Information), both pre-edge and most of the after-edge oscillations indicate a marked similarity to the spectrum of the CoO standard. Detecting further reduction of cobalt is more difficult, since the edge position remains unchanged. Nevertheless, as in the case of iron, the intensity changes of both the most intense peak and the pre-edge in electrode HEO-4 (Figure S5g, Supporting Information) indicate a contribution by metallic cobalt. While the spectrum of electrode HEO-5 is nearly the same as that of HEO-4, a further increase in the voltage causes the pre-peak intensity to decrease down to the value of CoO oxide standard in HEO-6 (Figure S5k, Supporting Information). The second discharge to 0.01 V replicates (and slightly surpluses) the pattern of HEO-4.

The Ni K-edge spectrum of the reduced electrode (HEO-2) almost replicates that of NiO standard (Figure S5d, Supporting Information), while in the subsequent SOCs, more reduced Ni species are detectable, as in the case of cobalt and iron. This is evident by comparing the Ni K-edge spectra of fully discharged (HEO-4) and fully charged (HEO-6) electrodes with those of metal and oxide standards (Figure S5h,l, Supporting Information).

Therefore, formation of metallic iron, cobalt and nickel is expected to occur. Although the metals in the HEO are not in their standard oxide phases, a linear combination fitting (LCF) analysis of the spectra of metal foils and oxide standards allows estimating the quantities of metal species with different oxidation states for each electrode. The case of Ni K-edge spectrum in electrodes HEO-4 and HEO-6 is shown as an example in Figure S6, Supporting Information, while Table S4, Supporting Information, reports the LCF outcomes for all electrodes. Figure S7, Supporting Information, shows the relative amounts of multi-valence

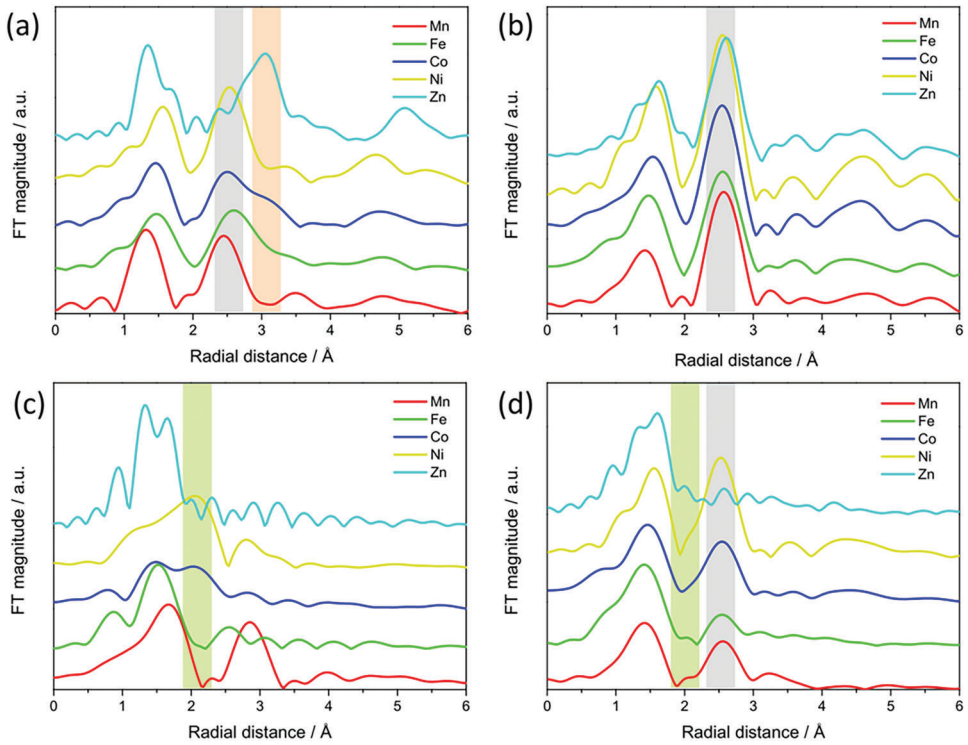

Figure 4. FT of the EXAFS for all metal K-edge in electrodes a) HEO-0, b) HEO-2, c) HEO-4, and d) HEO-6. Spectra are translated vertically for easier comparison. The gray and orange rectangles highlight the positions of the octahedral and tetrahedral sites, respectively; the green rectangles highlight the metal–metal first shell indicating formation of metallic species.

cationic species, correspondingly obtained for Fe, Co, and Ni. Finally, the resulting average oxidation state of these metals is displayed in Figure 3f. Although the first and second discharged electrodes exhibit quite similar spectral patterns, it is evident that formation of metallic species occurs to a greater extent during the second cycle. The largest relative amount of metallic species is observed for nickel (as shown in Figure S7c, Supporting Information, in the second cycle, metallic nickel exceeds 70% of Ni species).

The evolution of Zn K-edge XANES with the SOC (Figure S8a, Supporting Information) is similar to that reported for $ZnFe_2O_4$.[88] The oxidation state of zinc (2+) almost does not change during the charge and discharge process (Figure S8b,c, Supporting Information), and all electrodes except HEO-2 show very similar XANES curves. To gain a deeper insight on the role of Zn and its electroactivity (which is not related to charge change at the Zn site), Fourier transforms (FTs) of metal EXAFS signals, which are experimental indicators of the atomic environment of a given metal site, are compared to each other for all electrodes (**Figure 4**). The comparison is useful not only for the case of zinc, but also for the remaining metals. In a spinel-structured material, the metal cations can in principle occupy both octahedral and tetrahedral sites. XRD analysis does not allow distinguishing neighboring elements in the periodic table, which makes extremely difficult to determine the site distribution of each metal. Conversely, indications about the local coordination environment of each metal can be easily deduced via XAS, which is an element sensitive technique. Figure 4a displays the FTs corresponding to all metal cores for the fresh electrode. Two main peaks are clearly visible, ascribable to the first and second shell of ions around the photoabsorber (i.e. the metal whose K-edge core has been excited). The first atomic shell comprises oxygen anions for both octahedrally and tetrahedrally coordinated photoabsorbers, while the second shell comprises cations (metal–metal distance). In the FT of zinc, the second-shell peak is at a larger radial distance. As the distance between the metal in octahedral position to the nearest metal also in octahedral position ($M_O - M_O$) is smaller than that to the nearest metal in tetrahedral position ($M_O - M_T$), it can be argued that zinc is initially situated in tetrahedral position (Figure 4a), as expected. Going into more detail, iron and cobalt show a slope at the same distance as zinc, which indicates that a portion of them is also located in tetrahedral positions; this is in agreement to their pre-edge structure. In electrode HEO-2 (Figure 4b), however, the second shell for all metals (zinc included) has the same position, suggesting their uniform distribution, approximately at a distance of octahedral site. This indicates the migration of Zn from tetrahedral to octahedral position in the very first stage of the reduction, at potential as low as −0.9 V versus Li^+/Li. The phenomenon, allowed by the spinel structure that provides vacant sites within the lattice enabling lithium insertion and cation migration,[89] might be eased by the drastic reduction in activation barriers of room temperature diffusion of TMs in the presence of a high O_V concentration (40.6 at%).[90]

Migration of the Zn^{2+} cations from 8a to 16d sites during the initial stage of lithiation has already been reported for spinel $ZnFe_2O_4$.[88,89,91,92] At low Li-uptake, Li^+ ions show a preference for the vacant octahedral over vacant tetrahedral sites;[89] at higher Li-uptake, further insertion of Li^+ ions causes Zn^{2+}

cations to migrate to vacant octahedral (16c) sites to reduce electrostatic repulsion from Li^+ ions inserted into octahedral sites,[91,92] with the resulting structure allowing for easy Li-ion transport within channels no longer blocked by Zn^{2+} cations.[89] From HEO-3 onward, zinc shows the neighborhood of strongly distorted/disordered oxide species, with just the first coordination shell visible; therefore, the modification is not reversible. Distortions, caused by increased structural disorder due to lithiation, are also visible in the FTs of other metals. In discharged electrode spectra of Co and Ni, it is possible to identify the peak corresponding to the first shell metal-to-metal bond distance, indicating the formation of metallic species (Figure 4c). These phenomena are reversible during charging (Figure 4d). However, in the spectra of the second discharge (HEO-7), the effect is more marked and the characteristic shoulder starts to appear also for Fe (Figure S9a, Supporting Information). These results are in agreement with those obtained by LCF-XANES. The only metal that keeps the neighborhood similar throughout the cycle, with the only modification of the distance from the second shell, is manganese, again in fair agreement with the results of the LCF, which indicates Mn^{2+} as the most reduced form of Mn.

2.4. Phase Transformation of the Active Material

In spinel $CoMnFeO_4$ nanoparticles within LIB anodes, the movement of divalent cations from tetrahedral to neighboring octahedral positions is thought to be responsible for the phase transition from spinel to rock-salt structured $Co_{1/3}Mn_{1/3}Fe_{1/3}O$ that occurs during the early stage of reduction and is accompanied by formation of Li_2O.[93] Transition to rock-salt structure during reduction has been reported for several spinel (low- and high-entropy) oxides.[94–96] In order to investigate the occurrence of spinel to rock-salt phase transition in present (Mn,Fe,Co,Ni,Zn)-HEO NFs, ex situ XRD and MRS analyses were carried out on the electrodes extracted from LIBs. Figure S10a, Supporting Information, shows the XRD patterns of electrodes at different SOC.

In the as-prepared anode (Figure S10a, Supporting Information), the same reflections as in the active material are detected. Rietveld analysis (Figure S11a, Table S5, Supporting Information) confirmed the presence of a single spinel phase. In the electrode discharged to 0.9 V (HEO-2), the peaks originating from the spinel lattice weaken considerably and those peculiar to the rock-salt structure appear. Rietveld analysis (Figure S11b, Supporting Information) show the coexistence of a spinel phase (with somewhat larger cell size and strain) and a rock-salt phase with weight ratio approximately 1:2 (Table S5, Supporting Information).

MRS analysis carried out on different random locations within the electrode (Figure S12a, Supporting Information) confirms that the active material is no longer spatially uniform and two phases co-exist. The formation of the rock-salt phase is related to the increase of divalent cations during the discharge, as revealed by XAS. The XRD patterns of electrodes HEO-3 to HEO-5 comprise weak peaks from the rock-salt phase along with a set of peaks ($2\theta = 21.2°$, 23.2°, 30.3°, 31.5°, 33.8°, 39.6°), which should be ascribed to one or more unidentified phases. Some of the latter peaks are compatible with Li_2O and other ones with complex, spinel-based lithiated phases such as $Li_2Fe_3CoO_8$ (mp-758375). It is worthwhile stressing the similarity of the XRD patterns from HEO-3 to HEO-5, proving that no further phase transformation occurs at low voltage.

The fully charged electrode HEO-6, which resulted to be spatially uniform (Figure S12b, Supporting Information), comprises a spinel phase and a rock-salt phase with weight ratio approximately 1:3 (Table S5, Supporting Information). The peaks are much broader than those of HEO-2, because of higher strain (Table S6, Supporting Information); smaller crystallite size and amorphization could also contribute to the larger peak width. Finally, the diffractogram of HEO-7 is very similar to those of HEO-3 to HEO-5 as to both peak position and width.

2.5. Distribution of Cations in the Pristine NFs

The distribution of cations in the spinel lattice is difficult to ascertain, the more so for a 5-metal HEO. It has been shown in several cases that at thermal equilibrium the cation distribution among the 8a (tetrahedral) and 16d (octahedral) sites is determined by enthalpy (octahedral site stabilization) and that the cations are randomly distributed within each sub-lattice. Based on the EDX, XPS, and XAS results, and on simple consideration of electronegativity and crystal-field octahedral stabilization energy (OSPE),[36,97] the latter to partition cations between the 8a and 16d sub-lattices, an approximate, reasonable equilibrium cation distribution can be proposed for the pristine NFs. The elemental composition of the NFs can be approximated as $(Mn_{0.25}Fe_{0.1}Co_{0.2}Ni_{0.2}Zn_{0.25})_3O_4$ (see Figure 1f, XPS data). Both XPS and XAS (HEO-0) data show that Zn and Ni are present as divalent cations and Mn as tetravalent cation. Since Fe^{3+} is in general more stable than Co^{3+}, it can be safely assumed that Fe is only present as Fe^{3+}, whereas Co is present in both the +2 and +3 oxidation states. Under the constraint of electroneutrality, these considerations lead to the following composition: $(Mn^{4+}{}_{0.25}Fe^{3+}{}_{0.10}Co^{3+}{}_{0.05}Co^{2+}{}_{0.15}Ni^{2+}{}_{0.20}Zn^{2+}{}_{0.25})_3O_4$. Note that, due to the presence of tetravalent Mn cations, the fraction of divalent cations amounts to 1/2 instead of the usual 1/3 typical of the II-III spinels. Using OSPE values from literature,[97] it is easy to see that Mn^{4+}, $Co^{3+/2+}$, and Ni^{2+} cations reside in 16d sites, Zn^{2+} in 8a sites, and Fe^{3+} is found in both sublattices, as detailed in Table S6, Supporting Information, which gives the occupancy of the 8a and 16d sites. This equilibrium cation distribution (ECD, Figure S13a, Supporting Information) is at variance with XAS (HEO-0) results that support the presence of Mn, Fe, Co, and Ni in both 8a and 16d sub-lattices, based on i) the presence of pre-peaks in the XANES spectra (Figure S5, Supporting Information), and ii) the presence of significant shoulders at ≈3 Å in the FTs of Fe and Co edges (Figure 4a). The XAS data thus point to a more homogeneous partitioning of cations between the 8a and 16d sub-lattices. As a limiting case, the completely random cation distribution (CRCD, Figure S13b, Supporting Information), where each species is 1/3 in the 8a sub-lattice and 2/3 in the 16d sub-lattice, is shown in Table S7, Supporting Information. At the calcination temperature of 700 °C, the CRCD is less stable than the ECD by ≈65 kJ mol^{-1} (referred to a formula unit M_3O_4), as the latter is favored by ≈70 kJ mol^{-1} OSPE, which is not offset by the ≈5 kJ mol^{-1} unfavorable entropic term. The presence of Mn, Fe, Co, and Ni in both sub-lattices should then be attributed to the incomplete attainment of thermal equilibrium

during the 30-min calcination at 700 °C. Indeed, in the as-spun NFs, the spatial distribution of the cations is random, and it is reasonable that in the early stages of the oxide formation during calcination the cations are close to randomly distributed and they have to diffuse within the anion lattice framework to their preferred site. Thus, it seems that the pristine NFs have a cation distribution intermediate between the initial CRCD and the ECD toward which they are evolving.

Usually, the inversion degree λ of II-III spinels is defined as the fraction of trivalent cations in the 16d sublattice ($\lambda = 0$ in normal spinels and $\lambda = 1$ in inverse spinels.[56,98] Due to the presence of tetravalent Mn cations, this definition must be modified as follows: λ is the fraction of tetra- and trivalent-cations in the 16d sublattice. In the present case, $\lambda = 0.24$ for the ECD and $\lambda = 0.40$ for the CRCD. Thus, the pristine NFs are expected to display some degree of inversion, in agreement with the presence of the E_g' and A_{1g}' modes in the MRS of the pristine NFs.

3. Conclusions

Oxygen-deficient high-entropy (Mn,Fe,Co,Ni,Zn) oxide nanofibers with spinel structure are produced by electrospinning and evaluated as an anode material in lithium-ion batteries since we considered that the granular architecture of the $(Mn_{0.24}Fe_{0.11}Co_{0.21}Ni_{0.21}Zn_{0.23})_3O_4$ nanofibers and their inner channels are beneficial for the diffusion of Li ions.

Manganese, iron, cobalt, nickel, and zinc are present in the pristine NFs mainly as Mn^{4+}, Fe^{3+}, Co^{3+}/Co^{2+}, Ni^{2+}, and Zn^{2+} cations. The charge/discharge in anodes based on electrospun (Mn,Fe,Co,Ni,Zn) HEO NFs proceeds via lithium insertion, cation migration, and conversion reaction forming metals (and probably Li_2O or spinel-based lithiated oxides). However, as in the case of anodes based on different HEOs,[21] the reaction is not fully reversible and the reduction of cations to the metallic form is not complete. Iron, cobalt and nickel, initially present in the HEO lattice as Fe^{3+}, Co^{3+}/Co^{2+}, and $(Ni^{3+})/Ni^{2+}$ cations, undergo reduction to the metallic state, through a single-/multi-step reduction process. The relative amount of metallic species increases in the order iron < cobalt < nickel, both in the first (23%, 26%, and 55%, respectively) and second cycle (32%, 44%, and 71%, respectively). On the contrary, manganese, present in the pristine oxide as Mn^{4+} (and maybe Mn^{3+}), undergoes partial reduction to Mn^{3+}/Mn^{2+}, but upon re-oxidation, Mn^{4+} cations no longer appear, indicating the partial reversibility of the process and the occurrence of irreversible changes. Finally, Zn^{+2} cations do not electrochemically participate in the conversion lithiation/de-lithiation reaction of the (Mn,Fe,Co,Ni,Zn) HEO-based anode. However, they migrate along with the transition-metal cations from tetrahedral to octahedral positions. The migration, eased by the high O-vacancy concentration (40.6 at%), causes a phase transition from spinel to rock-salt. Cation migration from tetrahedral to octahedral positions facilitates Li-ion transport within channels opened in the oxide lattice[89] and possibly plays a stabilizing action for the oxide phase, in agreement with literature reports.[21]

This study provides a significant step forward made by a multi-technique approach to the understanding of high-entropy oxides, which is of great importance since these materials can potentially be utilized for the development of all components of rechargeable Li^+ and Na^+ ion batteries.[7,17–19] The reported results constitute a solid basis for the rational optimization of the preparation conditions of the (Mn,Fe,Co,Ni,Zn) HEO NFs to increase their stability and improve their electrochemical performance as active anode material in LIBs.

4. Experimental Section

Synthesis of the (Mn,Fe,Co,Ni,Zn)-HEO NFs: Manganese(II)acetate tetrahydrate, $Mn(CH_3COO)_2{\cdot}4H_2O$ (99%), iron (II) acetate, $Fe(CH_3COO)_2$ (95%), cobalt (II) acetate tetrahydrate, $Co(CH_3COO)_2{\cdot}4H_2O$ (99%), nickel (II) acetate tetrahydrate, $Ni(CH_3COO)_2{\cdot}4H_2O$ (98%), and zinc (II) acetate dehydrate, $(CH_3COO)_2Zn{\cdot}2H_2O$ (98%) were utilized as Mn, Fe, Co, Ni, and Zn sources for the synthesis of the HEO NFs. Polyacrylonitrile, $(C_3H_3N)_n$ (150 000 g mol^{-1}, 99.9%) and *N*,*N*-dimethylformamide, $HCON(CH_3)_2$ (anhydrous, 99.8%) were used to prepare the precursor polymer/solvent solution. All chemicals, supplied by Sigma-Aldrich (Table S8, Supporting Information), were utilized without further purification.

The HEO-NFs were prepared by electrospinning, following the procedure illustrated in detail in a previous paper[36] and briefly reported in the Supporting Information. The as-spun PAN/(Mn,Fe,Co,Ni,Zn)-acetates NFs were calcined in air to remove their organic components. Temperature was increased up to 700 °C at a fast rate (10 °C min^{-1}) and then kept constant for 30 min.

Characterization: SEM, HRTEM, XRD, MRS, and XPS analyses were carried out to investigate the morphology, texture, microstructure, crystalline phase, and surface composition of the (Mn,Fe,Co,Ni,Zn)-HEO NFs. Their electrochemical properties toward the Li-ion storage were studied by recording GCD and CV curves). Finally, to clarify the charge storage mechanism, ex situ synchrotron XAS analysis was conducted.

Morphology, Texture, Microstructure, Crystalline Phase, and Surface Composition of the NFs: The SEM images were acquired by a Phenom Pro-X scanning electron microscope, operated at 15 kV. HRTEM, high-angle annular dark-field scanning transmission electron microscopy (HAADF-STEM), SAED, and EDX elemental mappings were performed on a FEI Talos F200S scanning/transmission electron microscope, operated at 200 kV. Detailed information on the NF inner morphology was inferred from the projection analysis of STEM-EDX maps. Structural information about the primary particles was collected via the GPA of lattice fringes in the HRTEM images. For further details on projection analysis of the EDX elemental maps and GPA analysis see ref. [36] and Supporting Information.

A Bruker D2 diffractometer using Ni β-filtered Cu-K_α radiation source (λ = 0.1541 nm) was utilized to perform the XRD analysis. Selected diffractograms were analyzed by the Rietveld method using Maud 2.992 software. The crystallite size and microstrain effects were treated using an isotropic size-strain model with Delft line broadening.[99] Raman scattering was measured using a NTEGRA—Spectra SPM NT-MDT confocal microscope coupled to a solid-state laser operating at 2.33 eV (532 nm). To prevent local heating, spectra were recorded using a laser power of 250 μW at the sample surface. The scattered light from the sample, collected by means of a 100× Mitutoyo objective and dispersed by a 1800 lines mm^{-1} grating, was detected by a cooled ANDOR iDus CCD Camera. To evaluate the spatial homogeneity of the samples spectra from several random positions on each specimen were recorded. The average of the collected spectra provided a reliable picture of the entire sample. XPS spectra were acquired with an EnviroESCA instrument from Specs, equipped with an Al K_α excitation source ($h\nu$ = 1486.6 eV). Measurements were performed at a pressure of $\approx 10^{-6}$ mbar. The survey scan was obtained at 100 eV of pass energy, 1.0 eV•$step^{-1}$, and 0.1 s•$step^{-1}$. High resolution spectra were acquired at 50 eV pass energy, 0.1 eV•$step^{-1}$, and 0.1 s•$step^{-1}$. Binding energy (BE, uncertainty = ± 0.2 eV) values were corrected for charging attributing a BE value of 284.8 eV to the peak of C 1s of adventitious hydrocarbons, in agreement with the literature.[100] XPS curves were fitted with the

Keystone software provided by Specs, applying a Shirley-type background function.[101] Sensitivity factors of integrated peak areas used for quantification were provided by Specs. Further details on the instrumentation can be found elsewhere.[36]

Electrochemical Properties: In order to evaluate electrochemical properties of (Mn,Fe,Co,Ni,Zn)-HEO NFs, CR2032-type coin cells were assembled in an Ar-filled glovebox. For this purpose, active material (as-calcined HEO NFs), conductive carbon black (Super P, Timcal) and polyvinylidene fluoride (PVDF, Alfa Aesar) in mass ratio 7:2:1 were homogeneously mixed with *N*-methyl-2-pyrrolidone (NMP, anhydrous 99.5%, Sigma-Aldrich). The resulting slurry was uniformly cast on Cu foil (Goodfellow, UK) with a doctor blade apparatus. After drying in a vacuum oven at 60 °C for 1 h and cold-laminating, the electrodes (12 mm in diameter and 1.0–1.5 mg cm^{-2} in active material mass load) were die-cut and dried overnight at 90 °C under vacuum in a Büchi glass oven. Lithium metal foil was utilized as both counter and reference electrodes. 1 M $LiPF_6$ (ABCR, 99.9% battery grade) solution in a mixture of ethylene carbonate (EC, 99.9 %, ABCR), diethyl carbonate (DEC, 99.9%, ABCR), and dimethyl carbonate (DMC, 99.9%, ABCR) with 1:1:1 volume ratio was used as the electrolyte. A glass microfiber filter (Whatman) acted as a separator.

GCD cycling was carried out at room temperature using a CT2001A battery testing system (Landt Instruments). Cyclic voltammograms were measured on a Bio-Logic VMP3 multichannel potentiostat/galvanostat.

XAS Analysis: XAS experiments were conducted at XAFS beamline[102] in Elettra Synchrotron Trieste (Italy). The storage ring was operated at 2.0 GeV in top-up mode with a typical current 300 mA. Data were recorded at Fe, Mn, Co, Ni, and Zn K-edges in transmission mode. The electrodes studied ex situ in this experiment were detached from the Cu foil and were fixed on the sample holder with Kapton tape. Iron, manganese, cobalt, nickel, and zinc foils were used as internal references for the energy calibration in each scan. This allowed a continuous monitoring of the energy during consecutive scans. The white beam was monochromatized using a fixed exit monochromator equipped with a pair of Si (111) crystals. Spectra were collected with a constant k-step of nm^{-1} with 1 s per point acquisition time from 6244 to 7100 eV for Mn, from 6817 to 7672 eV for Fe, from 7514 to 8302 eV for Co, from 8138 to 8978 eV for Ni, and from 9467 to 10634 eV for Zn K-edges. XAS spectra were calibrated and analyzed using the Athena program.[103]

Supporting Information

Supporting Information is available from the Wiley Online Library or from the author.

Acknowledgements

C.T. and M.M. contributed equally to this work. Christoph Erdmann is acknowledged for transmission electron microscopy measurements. Measurements at ELETTRA were supported by the project #20220179. S.S. gratefully thanks the Italian Ministry of University and Research (MUR) for the financial support to this study through grant "PRIN 2017, 2017MCEEY4, Towards sustainable, high-performing, all-solid-state sodium-ion batteries." M.G., M.L., and M.M. acknowledge the partial funding from the National Recovery and Resilience Plan (NRRP), Mission 04 Component 2, Investment 1.5—NextGenerationEU, PE2 NEST—Network 4 Energy Sustainable Transition, Spoke 6 Energy Storage.

Conflict of Interest

The authors declare no conflict of interest.

Data Availability Statement

The data that support the findings of this study are available from the corresponding author upon reasonable request.

Keywords

anodes, ex situ XAS analysis, high-entropy spinel oxide, Li-ion batteries, Li-storage mechanism, nanofibers, spinel to rock-salt transition

Received: May 31, 2023
Revised: July 11, 2023
Published online:

[1] S. H. Yu, S. H. Lee, D. J. Lee, Y. E. Sung, T. Hyeon, *Small* **2016**, *12*, 2146.
[2] D. Wu, J. Song, Y. Ji, Q. Tian, Z. Sui, J. Chen, L. Yang, *J. Electroanal. Chem.* **2021**, *895*, 115531.
[3] S. Fang, D. Bresser, S. Passerini, in *Transition Metal Oxides for Electrochemical Energy Storage* (Eds: J. Nanda, V. Augustyn), Wiley, Hoboken, NJ **2022**, Ch. 4.
[4] B. Cantor, I. T. H. Chang, P. Knight, A. J. B. Vincent, *Mater. Sci. Eng., A* **2004**, *375*, 213.
[5] J. W. Yeh, S. K. Chen, S. J. Lin, J. Y. Gan, T. S. Chin, T. T. Shun, C. H. Tsau, S. Y. Chang, *Adv. Eng. Mater.* **2004**, *6*, 299.
[6] C. M. Rost, E. Sachet, T. Borman, A. Moballegh, E. C. Dickey, D. Hou, J. L. Jones, S. Curtarolo, J. P. Maria, *Nat. Commun.* **2015**, *6*, 8485.
[7] A. Sarkar, L. Velasco, D. Wang, Q. Wang, G. Talasila, L. de Biasi, C. Kübel, T. Brezenski, S. Bhattachrya, H. Hahn, B. Breitung, *Nat. Commun.* **2018**, *9*, 3400.
[8] A. Sarkar, Q. Wang, A. Schiele, M. R. Chellali, S. S. Bhattacharya, D. Wang, T. Brezenski, H. Hahn, L. Velasco, B. Breitung, *Adv. Mater.* **2019**, *31*, 1806236.
[9] A. Sarkar, B. Breitung, H. Hahn, *Scr. Mater.* **2020**, *187*, 43.
[10] T. Jin, X. Sang, R. R. Unocic, R. T. Kinch, X. Liu, J. Hu, H. Liu, S. Dai, *Adv. Mater.* **2018**, *30*, 1707512.
[11] J. Zhou, J. Zhang, F. Zhang, B. Niu, L. Lei, W. Wang, *Ceram. Int.* **2018**, *44*, 22014.
[12] R. Z. Zhang, F. Gucci, H. Zhu, K. Chen, M. J. Reece, *Inorg. Chem.* **2018**, *57*, 13027.
[13] S. Akrami, P. Edalati, M. Fuji, K. Edalati, *Mater. Sci. Eng., R* **2021**, *146*, 100644.
[14] M. Fu, X. Ma, K. Zhao, X. Li, D. Su, *iScience* **2021**, *24*, 102177.
[15] S. Y. Wang, T. Y. Chen, C. H. Kuo, C. C. Lin, S. C. Huang, M. H. Lin, C. C. Wang, H. Y. Chen, *Mater. Chem. Phys.* **2021**, *274*, 125105.
[16] M. Kheradmandfard, H. Minouei, N. Tsvetkov, A. K. Vayghan, S. F. Kashani-Bozorg, G. Kim, S. I. Hong, D. E. Kim, *Mater. Chem. Phys.* **2021**, *262*, 124265.
[17] D. Bérardan, S. Franger, A. K. Meena, N. J. Dragoe, *J. Mater. Chem. A* **2016**, *4*, 9536.
[18] Q. Wang, A. Sarkar, D. Wang, L. Velasco, R. Azmi, S. S. Bhattacharya, T. Bergfeldt, A. Düvel, P. Heitjans, T. Brezesinski, H. Hahn, B. Breitung, *Energy Environ. Sci.* **2019**, *12*, 2433.
[19] Y. Chen, H. Fu, Y. Huang, L. Huang, X. Zheng, Y. Dai, Y. Huang, W. Luo, *ACS Mater. Lett.* **2020**, *3*, 160.
[20] E. Lokcu, C. Toparli, M. Anik, *ACS Appl. Mater. Interfaces* **2020**, *12*, 23860.
[21] P. Ghigna, L. Airoldi, M. Fracchia, D. Callegari, U. Anselmi-Tamburini, P. D'angelo, N. Pianta, R. Ruffo, G. Cibin, D. O. de Souza, E. Quartarone, *ACS Appl. Mater. Interfaces* **2020**, *12*, 50344.
[22] N. Qiu, H. Chen, Z. Yang, S. Sun, Y. Wang, Y. Cui, *J. Alloys Compd.* **2019**, *777*, 767.
[23] F. Liu, M. Yu, X. Chen, J. Li, H. Liu, F. Cheng, *Chin. J. Catal.* **2022**, *43*, 122.
[24] J. Su, Z. Cao, Z. Jiang, G. Chen, Y. Zhu, L. Wang, G. Li, *Int. J. Appl. Ceram. Technol.* **2022**, *19*, 2004.

[25] C. Triolo, W. Xu, B. Petrovičovà, N. Pinna, S. Santangelo, *Adv. Funct. Mater.* **2022**, *32*, 2202892.
[26] H. Chen, N. Qiu, B. Wu, Z. Yang, S. Sun, Y. Wang, *RSC Adv.* **2019**, *9*, 28908.
[27] H. Chen, N. Qiu, B. Wu, Z. Yang, S. Sun, Y. Wang, *RSC Adv.* **2020**, *10*, 9736.
[28] Y. Wang, H. Li, H. Liu, L. Yang, C. Zeng, *Ceram. Int.* **2023**, *49*, 1940.
[29] H. Minouei, N. Tsvetkov, M. Kheradmandfard, J. Han, D. E. Kim, S. I. Hong, *J. Power Sources* **2022**, *549*, 232041.
[30] J. Dąbrowa, M. Stygar, A. Mikuła, A. Knapik, K. Mroczka, W. Tejchman, M. Danielewski, M. Martin, *Mater. Lett.* **2018**, *216*, 32.
[31] D. Wang, S. Jiang, C. Duan, J. Mao, Y. Dong, K. Dong, Z. Wang, S. Luo, Y. Liu, X. Qi, *J. Alloys Compd.* **2020**, *844*, 156158.
[32] A. Mao, F. Quan, H. Z. Xiang, Z. G. Zhang, K. Kuramoto, A. L. Xia, *J. Mol. Struct.* **2019**, *1194*, 11.
[33] B. Talluri, K. Yoo, J. Kim, *J. Environ. Chem. Eng.* **2022**, *10*, 106932.
[34] Z. Grzesik, G. Smoła, M. Miszczak, M. Stygar, J. Dąbrowa, M. Zajusz, K. Świerczek, M. Danielewski, *J. Eur. Ceram. Soc.* **2020**, *40*, 835.
[35] T. X. Nguyen, J. Patra, J. K. Chang, J. M. Ting, *J. Mater. Chem. A* **2020**, *8*, 18963.
[36] A. Ponti, C. Triolo, B. Petrovičovà, A. M. Ferretti, G. Pagot, W. Xu, V. Di Noto, N. Pinna, S. Santangelo, *Phys. Chem. Chem. Phys.* **2023**, *25*, 2212.
[37] B. Talluri, M. L. Aparna, N. Sreenivasulu, S. S. Bhattacharya, T. Thomas, *J. Energy Storage* **2021**, *42*, 103004.
[38] C. Triolo, S. Santangelo, B. Petrovičovà, M. G. Musolino, I. Rincón, A. Atxirika, S. Gil, Y. Belaustegui, *Appl. Sci.* **2023**, *13*, 721.
[39] B. Xiao, G. Wu, T. Wang, Z. Wei, Y. Sui, B. Shen, J. Qi, F. Wei, J. Zheng, *Nano Energy* **2022**, *95*, 106962.
[40] B. Xiao, G. Wu, T. Wang, Z. Wei, Z. Xie, Y. Sui, J. Qi, F. Wei, X. Zhang, L. B. Tang, J. C. Zheng, *ACS Appl. Mater. Interfaces* **2023**, *15*, 2792.
[41] T. Y. Chen, S. Y. Wang, C. H. Kuo, S. C. Huang, M. H. Lin, C. H. Li, H. Yi, T. Chen, C. C. Wang, Y. F. Liao, C. C. Lin, Y. M. Chang, J. W. Yeh, S. J. Lin, T. Y. Chen, H. Y. Chen, *J. Mater. Chem. A* **2020**, *8*, 21756.
[42] Z. Li, C. Wang, *One-Dimensional Nanostructures: Electrospinning Technique and Unique Nanofibers*, Springer, Heidelberg **2013**, pp. 15–29.
[43] Q. Liu, J. Zhu, L. Zhang, Y. Qiu, *Renewable Sustainable Energy Rev.* **2018**, *81*, 1825.
[44] S. Santangelo, *Appl. Sci.* **2019**, *9*, 1049.
[45] Y. Xing, W. Dan, Y. Fan, X. A. Li, *J. Mater. Sci. Technol.* **2022**, *103*, 215.
[46] W. Zhao, F. Yang, Z. Liu, H. Chen, Z. Shao, X. Zhang, K. Wang, L. Xue, *Ceram. Int.* **2021**, *47*, 29379.
[47] B. Petrovičovà, W. Xu, M. G. Musolino, F. Pantò, S. Patanè, N. Pinna, S. Santangelo, C. Triolo, *Appl. Sci.* **2022**, *12*, 5965.
[48] C. Triolo, S. Schweidler, L. Lin, G. Pagot, V. Di Noto, B. Breitung, S. Santangelo, *Energy Adv.* **2023**, *2*, 667.
[49] D. Wang, Z. Liu, S. Du, Y. Zhang, H. Li, Z. Xiao, W. Chen, R. Chen, Y. Wang, Y. Zou, S. Wang, *J. Mater. Chem. A* **2019**, *7*, 24211.
[50] A. Mullaliu, J. Asenbauer, G. Aquilanti, S. Passerini, M. Giorgetti, *Small Methods* **2020**, *4*, 1900529.
[51] A. Senthamizhan, B. Balusamy, Z. Aytac, T. Uyar, *CrystEngComm* **2016**, *18*, 6341.
[52] Y. Li, H. Zhang, X. Zhang, L. Wei, Y. Zhang, G. Hai, Y. Sun, *J. Mater. Sci.* **2019**, *30*, 15734.
[53] S. Santangelo, M. H. Raza, N. Pinna, S. Patanè, *Appl. Phys. Lett.* **2021**, *118*, 251105.
[54] Q. Hu, Z. Wang, X. Huang, Y. Qin, H. Yang, X. Ren, Q. Zhang, J. Liu, C. He, *Energy Environ. Sci.* **2020**, *13*, 5097.
[55] F. Mou, J. G. Guan, W. Shi, Z. Sun, S. Wang, *Langmuir* **2010**, *26*, 15580.
[56] M. Stygar, J. Dąbrowa, M. Moździerz, M. Zajusz, W. Skubida, K. Mroczka, K. Berent, K. Świerczek, M. Danielewski, *J. Eur. Ceram. Soc.* **2020**, *40*, 1644.
[57] B. Liang, Y. Ai, Y. Wang, C. Liu, S. Ouyang, M. Liu, *Materials* **2020**, *13*, 5798.
[58] V. M. Kaganer, B. Jenichen, M. Ramsteiner, U. Jahn, C. Hauswald, F. Grosse, S. Fernández-Garrido, O. Brandt, *J. Phys. D: Appl. Phys.* **2015**, *48*, 385105.
[59] H. D. Lutz, B. Müller, H. J. Steiner, *J. Solid State Chem.* **1991**, *90*, 54.
[60] Z. Wang, R. T. Downs, V. Pischedda, R. Shetty, S. K. Saxena, C. S. Zha, Y. S. Zhao, D. Schiferl, A. Waskowska, *Phys. Rev. B* **2003**, *68*, 094101.
[61] V. D'Ippolito, G. B. Andreozzi, D. Bersani, P. P. Lottici, *J. Raman Spectrosc.* **2015**, *46*, 1255.
[62] P. Choudhary, D. Varshney, *Mater. Res. Express* **2017**, *4*, 076110.
[63] B. Nandan, M. C. Bhatnagar, S. C. Kashyap, *J. Phys. Chem. Solids* **2019**, *129*, 298.
[64] M. A. Laguna-Bercero, M. L. Sanjuán, R. I. Merino, *J. Phys. Condens. Matter* **2007**, *19*, 186217.
[65] Z. Ž. Lazarević, Č. Jovalekić, A. Milutinović, D. Sekulić, V. N. Ivanovski, A. Rečnik, B. Cekić, N. Ž. Romčević, *J. Appl. Phys.* **2013**, *113*, 187221.
[66] M. H. Abdellatif, A. A. Azab, M. Salerno, *Mater. Res. Bull.* **2018**, *97*, 260.
[67] S. Supriya, S. Kumar, M. Kar, *J. Electron. Mater.* **2019**, *48*, 3612.
[68] W. Wang, Z. Ding, X. Zhao, S. Wu, F. Li, M. Yue, J. P. Liu, *J. Appl. Phys.* **2015**, *117*, 17A328.
[69] J. F. Moulder, W. F. Stickle, P. E. Sobol, K. D. Bomben, *Handbook of X-ray Photoelectron Spectroscopy: A Reference Book of Standard Spectra for Identification and Interpretation of XPS Data*, Physical Electronics Division, Perkin-Elmer Corporation, Eden Prairie, MN **1992**.
[70] R. O. Ansell, T. Dickinson, A. F. Povey, *Corros. Sci.* **1978**, *18*, 245.
[71] V. I. Nefedov, Y. V. Salyn, G. Leonhardt, R. Scheibe, *J. Electron. Spectrosc. Relat. Phenom.* **1977**, *10*, 121.
[72] G. C. Stevens, T. Edmonds, *J. Less-Common Met.* **1977**, *54*, 321.
[73] B. J. Tan, K. J. Klabunde, P. M. Sherwood, *J. Am. Chem. Soc.* **1991**, *113*, 855.
[74] K. S. Kim, N. Winograd, *Surf. Sci.* **1974**, *43*, 625.
[75] P. Lorenz, J. Finster, G. Wendt, J. V. Salyn, E. K. Žumadilov, V. I. Nefedov, *J. Electron Spectrosc. Relat. Phenom.* **1979**, *16*, 267.
[76] B. R. Strohmeier, D. M. Hercules, *J. Catal.* **1984**, *86*, 266.
[77] G. Deroubaix, P. Marcus, *Surf. Interface Anal.* **1992**, *18*, 39.
[78] J. P. Bonnelle, J. Grimblot, A. D'Huysser, *J. Electron Spectrosc. Relat. Phenom.* **1975**, *7*, 151.
[79] V. Nefedov, D. Gati, B. Dzhurinskii, N. Sergushin, Y. V. Salyn, *Zh. Neorg. Khim.* **1975**, *20*, 2307.
[80] G. Pagot, M. C. Cassani, F. Gambassi, B. Ballarin, D. Nanni, M. Coi, D. Barreca, E. Boanini, V. D. Noto, *Surf. Sci. Spectra* **2022**, *29*, 024007.
[81] J. Haber, J. Stoch, L. Ungier, *J. Electron Spectrosc. Relat. Phenom.* **1976**, *9*, 459.
[82] B. J. Tan, K. J. Klabunde, P. M. A. Sherwood, *J. Am. Chem. Soc.* **1991**, *113*, 855.
[83] C. Y. Huang, C. W. Huang, M. C. Wu, J. Patra, T. X. Nguyen, M. T. Chang, O. Clemens, J. M. Ting, J. Li, J. K. Chang, W. W. Wu, *Chem. Eng. J.* **2021**, *420*, 129838.
[84] M. Bijelić, X. Liu, Q. Sun, A. B. Djurišić, M. H. Xie, A. M. Ng, C. Suchomski, I. Djerdj, Ž. Skoko, J. Popović, *J. Mater. Chem. A* **2015**, *3*, 14759.
[85] G. Zhang, L. Yu, H. B. Wu, H. E. Hoster, X. W. Lou, *Adv. Mater.* **2012**, *24*, 4609.
[86] H. Song, L. Shen, C. J. Wang, *J. Mater. Chem. A* **2014**, *2*, 20597.
[87] J. Rissler, K. Klementiev, J. Dahl, B. M. Steenari, M. Edo, *Energy Fuels* **2020**, *34*, 14505.

[88] Y. Zhang, C. J. Pelliccione, A. B. Brady, H. Guo, P. F. Smith, P. Liu, A. C. Marschilok, K. J. Takeuchi, E. S. Takeuchi, *Chem. Mater.* **2017**, *29*, 4282.
[89] K. R. Tallman, P. J. West, S. Yan, S. Yao, C. D. Quilty, F. Wang, A. C. Marschilok, D. C. Bock, K. J. Takeuchi, E. S. Takeuchi, *Nanotechnology* **2021**, *32*, 375403.
[90] D. Qian, B. Xu, M. Chi, Y. S. Meng, *Phys. Chem. Chem. Phys.* **2014**, *16*, 14665.
[91] M. Ciambezi, *Ph.D. Thesis*, Camerino University **2019**.
[92] D. Spada, M. Ambrosetti, M. C. Mozzati, B. Albini, P. Galinetto, A. Cini, M. Fittipaldi, M. Bini, *Mater. Res. Bull.* **2023**, *160*, 112132.
[93] S. Permien, S. Indris, A. L. Hansen, M. Scheuermann, D. Zahn, U. Schürmann, G. Neubüser, L. Kienle, E. Yegudin, W. Bensch, *ACS Appl. Mater. Interfaces* **2016**, *8*, 15320.
[94] S. Permien, S. Indris, U. Schürmann, L. Kienle, S. Zander, S. Doyle, W. Bensch, *Chem. Mater.* **2016**, *28*, 434.
[95] Y. Zheng, X. Wu, X. Lan, R. Hu, *Processes* **2021**, *10*, 49.
[96] J. Patra, T. X. Nguyen, C. C. Tsai, O. Clemens, J. Li, P. Pal, W. K. Chan, C. H. Lee, H. Y. T. Chen, J. M. Ting, J. K. Chang, *Adv. Funct. Mater.* **2022**, *32*, 2110992.
[97] A. F. Wells, *Structural Inorganic Chem.*, Clarendon Press, Oxford **2012**.
[98] B. Issa, I. M. Obaidat, B. A. Albiss, Y. Haik, *Int. J. Mol. Sci.* **2013**, *14*, 21266.
[99] L. Lutterotti, P. Scardi, *J. Appl. Cryst.* **1990**, *23*, 246.
[100] D. Briggs, M. P. Seah, *Practical Surface Analysis: Auger and X-ray Photoelectron Spectroscopy*, 2nd ed., John Wiley & Sons, New York **1990**.
[101] D. A. Shirley, *Phys. Rev. B* **1972**, *5*, 4709.
[102] G. Aquilanti, M. Giorgetti, R. Dominko, L. Stievano, I. Arčon, N. Novello, L. Olivi, I. Ar, N. Novello, L. Olivi, I. Arčon, N. Novello, L. Olivi, *J. Phys. D: Appl. Phys.* **2017**, *50*, 074001.
[103] B. Ravel, M. Newville, *J. Synchrotron Rad.* **2005**, *12*, 537.

